

## Article

# Perovskite/Pyrochlore Composite Mineral-like Ceramic Fabrication for $^{90}\text{Sr}/^{90}\text{Y}$ Immobilization Using SPS-RS Technique

Evgeniy K. Papynov <sup>1,\*</sup>, Oleg O. Shichalin <sup>1,\*</sup>, Anton A. Belov <sup>1</sup>, Igor Yu. Buravlev <sup>1</sup>, Alexey Zavjalov <sup>2</sup>, S. A. Azon <sup>1</sup>, Alexander N. Fedorets <sup>1</sup>, Zlata E. Kornakova <sup>1</sup>, Aleksey O. Lembikov <sup>1</sup>, E. A. Gridasova <sup>1</sup>, Andrei Ivanets <sup>3</sup> and Ivan G. Tananaev <sup>1,4</sup>

<sup>1</sup> Nuclear Technology Laboratory, Department of Nuclear Technology, Institute of High Technologies and Advanced Materials, Far Eastern Federal University, 10 Ajax Bay, Russky Island, Vladivostok 690922, Russia; nefryty@gmail.com (A.A.B.); buravlev.i@gmail.com (I.Y.B.); azon.sa@dvfu.ru (S.A.A.); fedorets.alexander@gmail.com (A.N.F.); kornakova.ze@students.dvfu.ru (Z.E.K.)

<sup>2</sup> Institute of Solid-State Chemistry and Mechanochemistry, Siberian Branch, Russian Academy of Sciences, 18 Kutateladze Street, Novosibirsk 630128, Russia; zav\_alexey@list.ru

<sup>3</sup> Institute of General and Inorganic Chemistry of National Academy of Sciences of Belarus, Surganova St. 9/1, 220072 Minsk, Belarus; andreiiivanets@yandex.by

<sup>4</sup> Institute of Chemistry and Technology of Rare Elements and Mineral Raw Materials, Kola Science Center, Russian Academy of Sciences, Akademgorodok, 26a, Apatity 184209, Russia

\* Correspondence: papynov@mail.ru (E.K.P.); oleg\_shich@mail.ru (O.O.S.)

**Abstract:** A novel solid-phase synthetic approach was developed to produce a mineral-like composite ceramic based on strontium titanate ( $\text{SrTiO}_3$ ) and yttrium titanate ( $\text{Y}_2\text{Ti}_2\text{O}_7$ ) matrices for immobilizing radionuclides such as  $^{90}\text{Sr}$  and its daughter product  $^{90}\text{Y}$ , as well as lanthanides and actinides, via reactive spark plasma sintering technology (SPS-RS). Using XRD, SEM, and EDS analyses, the sintering kinetics of the initial mixed oxide reactants of composition  $\text{Y}_x\text{Sr}_{1-1.5x}\text{TiO}_3$  ( $x = 0.2, 0.4, 0.6$  and  $1$ ) and structure-phase changes in the ceramics under SPS-RS conditions were investigated as a function of  $\text{Y}^{3+}$  content. In addition, a detailed study of phase transformation kinetics over time as a function of the heating temperature of the initial components ( $\text{SrCO}_3$ ,  $\text{TiO}_2$ , and  $\text{Y}_2\text{O}_3$ ) was conducted via in situ synchrotron XRD heating experiments. The composite ceramic achieved relatively high physicomechanical properties, including relative density between  $4.92\text{--}4.64\text{ g/cm}^3$ , Vickers microhardness of  $500\text{--}800\text{ HV}$ , and compressive strength ranging from  $95.5\text{--}272.4\text{ MPa}$ . An evaluation of hydrolytic stability and leaching rates of  $\text{Sr}^{2+}$  and  $\text{Y}^{3+}$  from the matrices was performed, demonstrating rates did not exceed  $10^{-5}\text{--}10^{-6}\text{ g}\cdot\text{cm}^{-2}\cdot\text{day}^{-1}$  in compliance with GOST R 50926-96 and ANSI/ANS 16.1 standards. The leaching mechanism of these components was studied, including the calculation of solution penetration depth in the ceramic bulk and ion diffusion coefficients in the solution. These findings show great promise for radioactive waste conditioning technologies and the manufacturing of radioisotope products.

**Keywords:** ceramic; matrices; radionuclides; strontium; yttrium; radioactive waste; ionizing irradiation sources; spark plasma sintering; reactive synthesis; solid-phase synthesis



**Citation:** Papynov, E.K.; Shichalin, O.O.; Belov, A.A.; Buravlev, I.Y.; Zavjalov, A.; Azon, S.A.; Fedorets, A.N.; Kornakova, Z.E.; Lembikov, A.O.; Gridasova, E.A.; et al. Perovskite/Pyrochlore Composite Mineral-like Ceramic Fabrication for  $^{90}\text{Sr}/^{90}\text{Y}$  Immobilization Using SPS-RS Technique. *Coatings* **2023**, *13*, 2027. <https://doi.org/10.3390/coatings13122027>

Academic Editor: Victor J. Rico

Received: 8 November 2023

Revised: 24 November 2023

Accepted: 28 November 2023

Published: 30 November 2023



**Copyright:** © 2023 by the authors. Licensee MDPI, Basel, Switzerland. This article is an open access article distributed under the terms and conditions of the Creative Commons Attribution (CC BY) license (<https://creativecommons.org/licenses/by/4.0/>).

## 1. Introduction

The radioactive isotope  $^{90}\text{Sr}$  finds wide application across various science, technology, and medicine fields. Production of  $^{90}\text{Sr}$  occurs via the fission of  $^{235}\text{U}$  and  $^{239}\text{Pu}$  in nuclear reactors.  $^{90}\text{Sr}$  emits beta radiation with an energy of  $0.546\text{ MeV}$  and has a half-life of  $28.8\text{ years}$  [1]. Upon decay,  $^{90}\text{Sr}$  forms  $^{90}\text{Y}$ , a strong beta emitter with an energy of  $2.28\text{ MeV}$  and a half-life of  $64\text{ h}$  [2]. The unique radiative characteristics of these radionuclides determine their extensive utilization in nuclear energy, medicine, industry, and scientific research. Specifically, an important use of  $^{90}\text{Sr}$  and  $^{90}\text{Y}$  is in radioisotope thermoelectric

generator (RITEG) constructions as autonomous sources of electric power employed in space applications as well as ground-based navigation systems and meteorological stations [3,4]. In addition, these radionuclides are widely leveraged to develop sources of ionizing radiation (IRS) in radiation technology. In medicine, compounds of  $^{90}\text{Sr}$  and  $^{90}\text{Y}$  are applied in the diagnosis and radiotherapy of cancerous conditions [5,6].

The high radiological hazard presented by  $^{90}\text{Sr}$  and  $^{90}\text{Y}$  necessitates reliable isolation of these radionuclides from direct contact with users of relevant devices and the surrounding environment. Accordingly, significant focus is devoted to developing effective solid matrix materials for their secure immobilization. The most promising materials for these purposes are ceramic materials and their composites, which confer several advantages relative to alternative glass matrixes [7–9]. In particular, ceramic matrices have higher chemical stability compared to glasses. Ceramics also have higher thermal and radiation resistance, which increases the long-term reliability of radioactive waste immobilization. Another advantage of ceramic matrices is their higher mechanical strength, which is important for the safe transportation and disposal of waste. In addition, the use of ceramics provides a greater variety of compositions for the immobilization of different types of radionuclides. Finally, the use of powder metallurgy allows the production of denser and more homogeneous matrices with ceramics, which is critical for the long-term stability of immobilization [10–15]. Promising ceramic matrices for  $^{90}\text{Sr}$  are mineral-like compounds based on titanates, zirconates, phosphates, and silicates. The potential of complex oxides with perovskite, pyrochlore, zirconolite, and monazite structures has been widely studied [16,17]. For example, the synthesis of  $\text{SrTiO}_3$  ceramic possessing a perovskite crystal structure is of particular interest. Within these compounds, strontium ions (and others) are incorporated into the structure in place of calcium ions, forming stable solid solutions [18–21]. The regular crystalline lattice securely retains radionuclides within its nodes, preventing migration into the surrounding environment. In this regard, industrial experience exists utilizing  $\text{SrTiO}_3$  in RITEG production [22].

It is important to consider that the matrix properties are also influenced by the synthesis method. Conventional methods rely upon high-temperature sintering of powder mixtures, which may first be cold-pressed into compacted green bodies over several hours or days. This approach can result in significant energy expenditures as well as the possible generation of secondary wastes in the gas phase. It may also reduce the quality of the final product and lead to equipment degradation over time. Alternative processing routes could help to address such issues and are worth further exploration. Continued development of material fabrication techniques aims to promote sustainability, efficiency, and consistency in product quality.

As an alternative to conventional methods, scientists have explored spark plasma sintering technology (SPS) [23–25]. SPS is based on heating the compact through pulsed electric current under uniaxial pressing conditions, with high heating rates and short processing times measured in minutes. In particular, the potential of SPS has been experimentally demonstrated for synthesizing pyrochlore structure ceramic [26], scheelite [27–29], feldspar-like [30], sodium zirconium phosphate (NZP) [31], and glass-ceramic composites for immobilizing  $^{90}\text{Sr}$  [32–36]. Additionally, our work has initially demonstrated high promise for applying SPS to produce a mineral-like  $\text{SrTiO}_3$  perovskite matrix for  $^{90}\text{Sr}$  immobilization, as well as to fabricate a prototype of IRS based on this approach [37]. SPS shows potential as a lower-energy and more efficient alternative processing route.

Among the more attractive methods is the process of synthesizing  $\text{SrTiO}_3$  ceramic via reactive spark plasma sintering (SPS-RS) [38]. In this case, ceramic formation with the required composition occurs via solid-phase reaction in situ interaction of the initial powders during spark plasma heating. Our experiments [39] demonstrated that brief heating at relatively low temperatures serves to minimize the loss of volatile components from the original mixture. The resultant ceramic possesses a fine-grained, dense microstructure with high mechanical properties and hydrolytic durability. A prototype radiation source fabricated using this ceramic demonstrates superior operating characteristics compared to

regulatory standards and analogous devices [40]. SPS-RS enables efficient, low-temperature synthesis with optimal material performance.

Considering the dual nature of  $^{90}\text{Sr}$  existing together with its daughter product  $^{90}\text{Y}$ , it is important to account for the ceramic matrix's crystalline phase composition relative to both radionuclides. In this vein, the aim of the present study was to investigate the solid-phase synthesis of a mineral-like strontium-containing ceramic based on the  $\text{SrTiO}_3$  perovskite composition containing varying  $\text{Sr}^{2+}/\text{Y}^{3+}$  ratios via SPS-RS. Investigations were supplemented by examining phase transformation dynamics in the solid state with high temporal resolution using in situ synchrotron XRD heating experiments. This enables the determination of temperature ranges for phase formation, assessment of solid-state reaction rates, identification of possible intermediate compounds within the ceramic, and elucidation of influences on performance characteristics. Establishing optimal synthesis parameters can yield materials with tailored properties necessary for reliable immobilization of  $^{90}\text{Sr}$ ,  $^{90}\text{Y}$ , and other radionuclides. Such research had not been previously conducted.

## 2. Materials and Methods

### 2.1. Reagents

The reaction mixtures (RM) were fabricated using powders of strontium carbonate ( $\text{SrCO}_3$ ), titanium dioxide ( $\text{TiO}_2$ ), and yttrium oxide ( $\text{Y}_2\text{O}_3$ ) (99.9%, Sigma-Aldrich, St. Louis, MI, USA).

### 2.2. Synthesis of Initial Powders Reaction Mixtures

The RM were prepared by mechanochemical mixing of the starting powders in a planetary ball mill in a single 10 min cycle at 870 rpm. Zirconium dioxide milling jars and milling bodies were used for homogenization.

The quantitative mass ratios of initial reagents are presented in Table 1.

**Table 1.** Chemical composition of starting reaction mixtures.

Initial Reagents	Ratio			
	$\text{Y}_x\text{Sr}_{1-1.5x}\text{TiO}_3$ , x = 0.2	$\text{Y}_x\text{Sr}_{1-1.5x}\text{TiO}_3$ , x = 0.4	$\text{Y}_x\text{Sr}_{1-1.5x}\text{TiO}_3$ , x = 0.6	$\text{Y}_x\text{Sr}_{1-1.5x}\text{TiO}_3$ , x = 1
$\text{Y}_2\text{O}_3$	1.28	2.70	4.28	4.84
$\text{TiO}_2$	4.56	4.79	5.05	5.15
$\text{SrCO}_3$	5.90	3.54	0.93	-

### 2.3. Spark Plasma Sintering Reactive Synthesis of Ceramic Materials

Ceramic samples were synthesized via SPS-RS using a Dr.Sinter·LAB™ SPS-515S system (Japan, Kyoto) according to the general procedure: 4 g of RM powder was placed in a graphite die (working diameter 15.5 mm), pre-consolidated (pressure 20.7 MPa), then transferred to a vacuum chamber ( $10^{-5}$  atm). Heating was achieved using unipolar low-voltage pulsed current in On/Off mode, with a 12 pulse/2 pause periodicity, resulting in a pulse packet duration of 39.6 ms and pause of 6.6 ms. The temperature during SPS was monitored using an optical pyrometer (lower limit 650 °C) focused on a hole in the outer wall of the die 5.5 mm deep. The heating rate was controlled in stages: 300 °C/min from 0 to 650 °C, then 50 °C/min above 650 °C (working range of pyrometer). Samples were held at maximum temperature for 5 min, and then cooled to room temperature over 30 min. Consolidation pressure was 21.5 MPa. Graphite foil (200 μm thick) was used to prevent adhesion and facilitate sample removal. Insulating cloth wrapped the die to minimize heat loss. The resultant cylindrical matrix samples measured 15.3 mm diameter and 4–6 mm height, depending on sintering parameters.

#### 2.4. Characterization of the Research Methods

Particulate size distribution (PSD) of the RM powder was determined using a G3-ID unit of Malvern Instruments Ltd. (Malvern, UK). Scanning electron microscopy (SEM) was carried out using a Carl Zeiss CrossBeam 1540 XB (Jena, Germany) equipped with a Bruker energy dispersive X-ray spectroscopy (EDS) attachment (Mannheim, Germany). X-ray powder diffraction (XRD) analysis was conducted using Bruker D8 Advance (Mannheim, Germany) and Burevestnik Colibri (Moscow, Russia) diffractometers with  $\text{CuK}\alpha 1\text{-K}\alpha 2$  radiation (40 kV, 10 mA; mean wavelength  $\lambda = 1.5418 \text{ \AA}$ ). The signal was detected using a Muthen2 detector with a  $\text{K}\beta$  Ni-filter, over a  $2\theta$  range of  $20\text{--}100^\circ$ , step size  $0.0185^\circ$  and dwell time per step of 244 s. Vickers microhardness (HV) was measured at 0.2 N load using a Shimadzu HMV-G-FA-D microhardness tester (Kyoto, Japan). Compressive strength ( $\sigma_{cs}$ ) was studied using a Shimadzu Autograph AG-X plus 100 kN universal testing machine (Kyoto, Japan). Sample bulk relative density (RD) was determined using hydrostatic weighing on an OHAUS Corporation Adventurer<sup>TM</sup> balance (Parsippany, NJ, USA).

Hydrolytic durability of the matrices was assessed based on the leaching rate of strontium ions during prolonged contact (30 days) with distilled water (pH 6.8) at room temperature ( $25^\circ\text{C}$ ) under static conditions according to GOST R 52126-2003, analogous to ANSI/ANS 16.1, which was updated in accordance with an earlier version recommended by the IAEA (ISO 6961:1982). The strontium ion concentration was determined using inductively coupled plasma mass spectrometry (ICP-MS) on a Thermo Scientific iCAP 7600 Duo spectrometer (Waltham, MA, USA).

The leaching rates are calculated according to the following equation:

$$R_n^{\text{Sr}} = \frac{m_n^{\text{Sr}}}{M_0^{\text{Sr}} \times t_n \times S} \quad (1)$$

where  $R_n^{\text{Sr}}$ —Sr leaching rate ( $\text{g}/\text{cm}^2 \cdot \text{day}$ );  $m_n^{\text{Sr}}$ —Sr mass, leached for  $n$ th time interval, g;  $M_0^{\text{Sr}}$ —Sr mass concentration in the matrix,  $\text{g}/\text{g}$ ;  $S$ —sample's surface area,  $\text{cm}^2$ ;  $t_n$ —duration of the  $n$ th time interval, days.

The calculation of the effective diffusion coefficient ( $D_e$ ) was performed using mathematical transformations of the second Fick law according to the method described in the paper [41]:

$$\frac{\sum m}{M_0} = 2 \left( \frac{D_e}{\pi} \right)^{\frac{1}{2}} \times \left( \frac{S}{V} \right) t^{\frac{1}{2}} + \alpha \quad (2)$$

where  $m$ —strontium weight, mg;  $t$ —leaching time, s;  $M_0$ —initial cesium content in the sample, mg;  $D_e$ —effective diffusion coefficient,  $\text{cm}^2/\text{s}$ ;  $S$ —the surface area of the sample,  $\text{cm}^2$ ;  $V$ —a volume of sample,  $\text{cm}^3$ ;  $\alpha$ —parameter that takes into account the initial leaching of strontium, not related to diffusion (strontium leaches out at the initial contact of the leaching solution with the sample surface).

In the calculation, this equation was reduced to a linear form by introducing the coefficient  $K$ , which represents the tangent of the slope of the straight-line dependence of strontium leaching from the sample on the square root of the contact time of the material with the leaching agent:

$$K = 2 \left( \frac{D_e}{\pi} \right)^{0.5} \times \left( \frac{S}{V} \right) \quad (3)$$

The effective diffusion coefficient was calculated:

$$D_e = \frac{K^2 \times \pi}{4} \times \left( \frac{V}{S} \right)^2 \quad (4)$$

The leaching index ( $L$ ) was calculated as the decimal logarithm of the inverse diffusion value:

$$L = \lg \frac{1}{D_e} \quad (5)$$

Estimation of the dominant leaching mechanism based on the dependence of the decimal logarithm of the accumulated fraction of leached radionuclide ( $B_t$ , mg/m<sup>2</sup>) on the decimal logarithm of the leaching time  $t$ , s:

$$\lg(B_t) = \frac{1}{2} \lg t + \lg \left[ U_{\max} d \sqrt{\frac{D_e}{\pi}} \right] \quad (6)$$

where is  $U_{\max}$ —the maximum amount of leached radionuclide, mg/kg,  $d$ —matrix density, kg/m<sup>3</sup>.

The leaching depth of the matrix characterizes the destruction of the matrix.

Matrix when it is in aqueous medium and is calculated according to Equation (7):

$$L_t^i = \sum_i^n \left( W_n^i \frac{t_n}{d} \right) \quad (7)$$

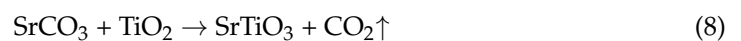
where is  $L_t^i$ —the leaching depth of the matrix reached during the time interval  $t_n$ , cm;  $d$ —density of the sample, g/cm<sup>3</sup>.

### 2.5. In Situ Synchrotron Study

In situ synchrotron radiation (SR) XRD heating experiments were performed using beamline 5-B at the VEPP-3 storage ring [42] at the Siberian Centre for Synchrotron and Terahertz Radiation (SB RAS, Novosibirsk, Russia) based on the VEPP-4-VEPP-2000 electron-positron collider complex at the Budker Institute of Nuclear Physics of Siberian Branch of the Russian Academy of Sciences [43]. Diffraction patterns were recorded using a one-dimensional detector OD-3 [44]. The wavelength of monochromatic radiation was 1.51 Å over a  $2\theta$  range of 18–50°. Samples were placed in a special furnace heated at a constant rate of 15 °C/min to 400 °C and 5 °C/min to 1000 °C. The OD-3 exposure time was set to 60 s.

## 3. Results and Discussion

The ceramic formation was based on the initiation of a chemical reaction according to the in situ interaction principle of the starting RM powders during spark plasma sintering, according to the following parallel reactions:



According to the granulometric analysis data of the RM (Figure 1), all initial powders were found to have a polydisperse composition. SrCO<sub>3</sub> has particles in the size range of 0.2–5 μm and an insignificant amount (about 10%) in the range of 20–50 μm (Figure 1a). TiO<sub>2</sub> is represented by four particle size distribution areas in the ranges of 0.1–1 μm in the amount of 15 vol.%, 1–5 μm 25 vol.%, 5–20 μm 30 vol.%, and 20–50 μm with 30 vol.% (Figure 1b). Y<sub>2</sub>O<sub>3</sub> has four particle size distribution areas in the ranges of 0.1–0.5 μm in the amount of 5 vol.%, 0.5–5 μm 25 vol.%, 5–20 μm 50 vol.%, and 20–100 μm with 20 vol.% (Figure 1c).

The reaction mixtures (RM) (Figure 2a–d) with varying ratios of TiO<sub>2</sub>, Y<sub>2</sub>O<sub>3</sub>, and SrCO<sub>3</sub> following high-energy grinding comprised particles sized 0.1–1 μm. According to SEM images, the RM consisted of agglomerations of nanoparticles less than 100 nm (Figure 3a–d) as determined using EDS. Elemental mapping of RM particle surfaces from EDS (Figure 3a–d) indicated a uniform composition without foreign inclusions, corroborated using XRD analysis (Figure 4). With the changes in component contents outlined in Table 1, decreasing SrCO<sub>3</sub> concentration reduced XRD peak intensities with an inverse dependence observed for Y<sub>2</sub>O<sub>3</sub>.

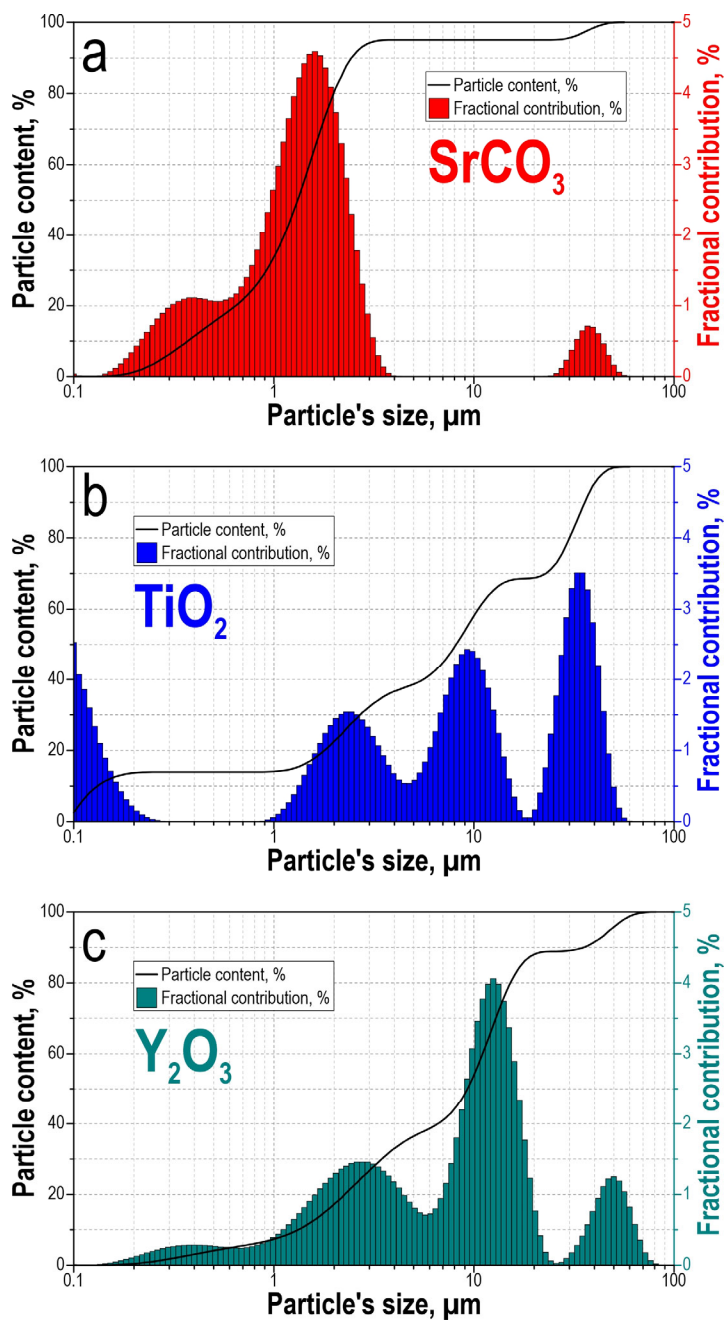


Figure 1. Fractional composition of initial reagents: (a)— $\text{SrCO}_3$ ; (b)— $\text{TiO}_2$ ; (c)— $\text{Y}_2\text{O}_3$ .

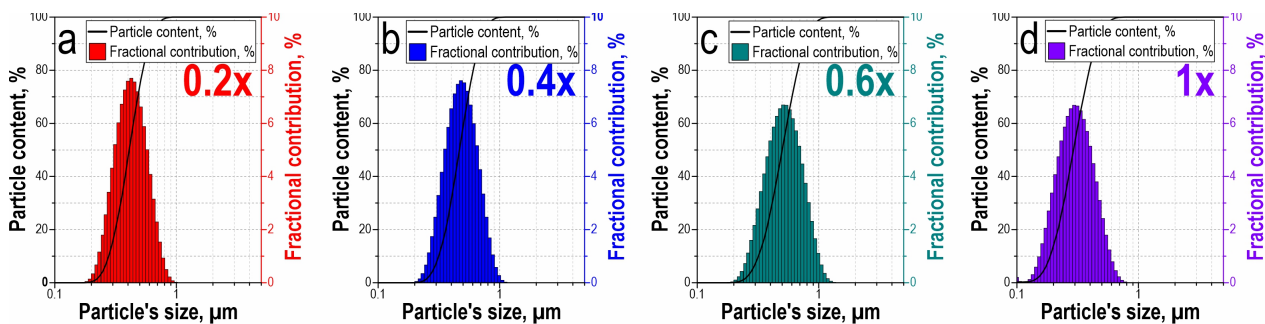
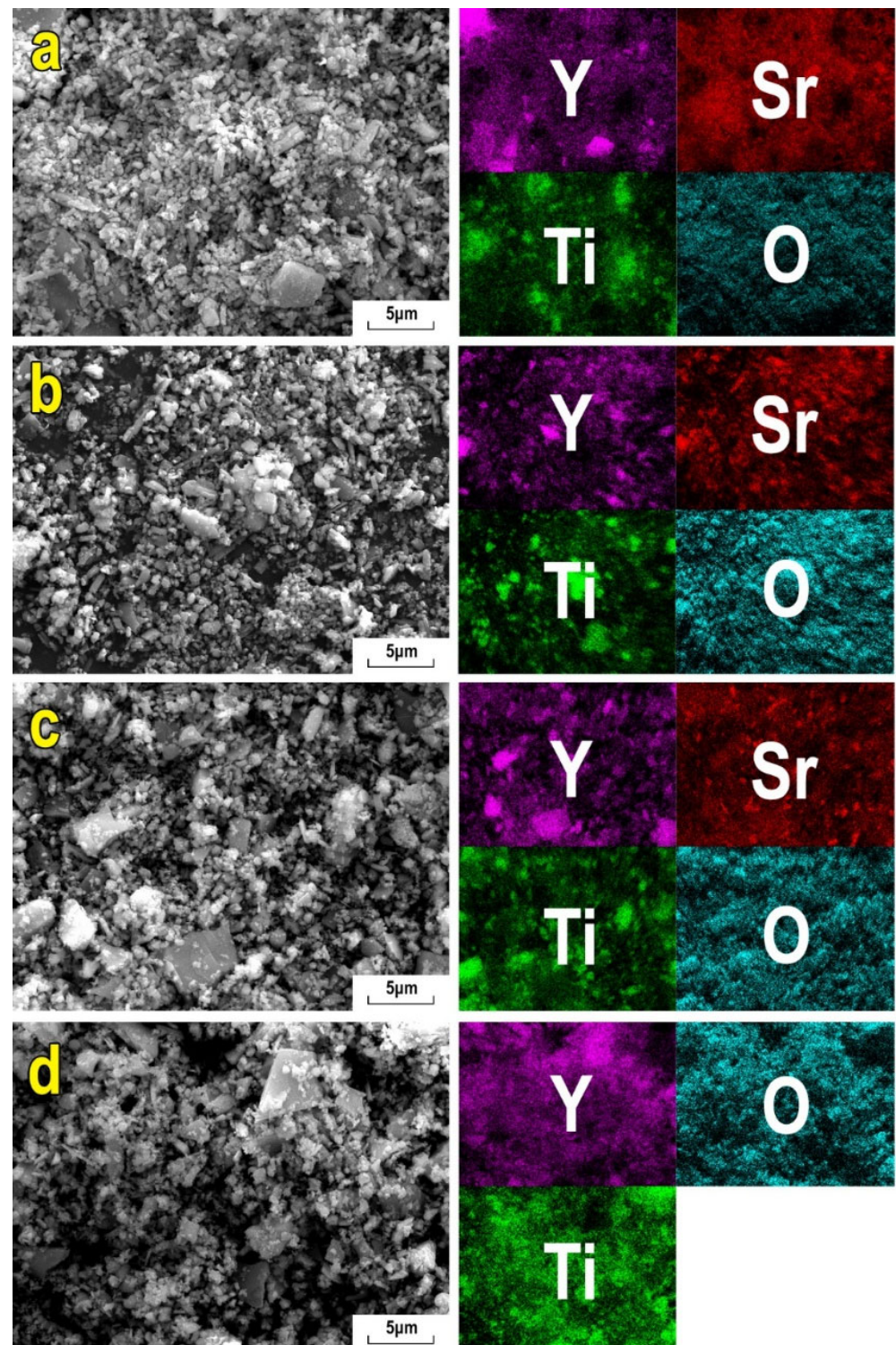
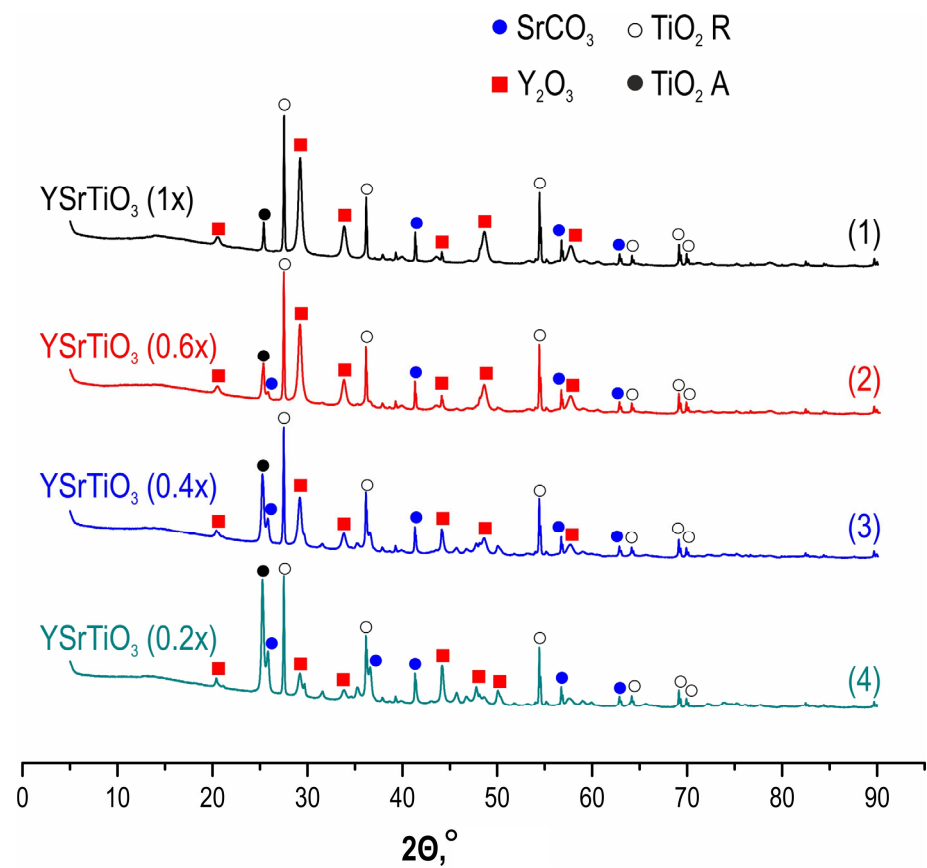


Figure 2. Fractional composition of RM  $\text{Sr}_{1-1.5x}\text{Y}_x\text{TiO}_3$  ( $x = 0.2, 0.4, 0.6$  and  $1$ ).



**Figure 3.** SEM micrographs and EDS analyses of reaction mixture powders of composition  $Y_xSr_{1.5-x}TiO_3$ : (a)— $x = 0.2$ ; (b)— $x = 0.4$ ; (c)— $x = 0.6$ ; (d)— $x = 1$ .

X-ray diffraction analysis of the  $Y_xSr_{1.5-x}TiO_3$  reaction mixture powders revealed the presence of orthorhombic  $SrCO_3$  crystalline phase with space group  $Pm\bar{c}n$  (DB# 01-078-4340), tetragonal  $TiO_2$  phases with space group  $P42/mnm$  for Rutile (DB# 01-079-5859) and  $I41/amd$ , choice-2 for Anatase (DB# 01-076-3177), and cubic  $Y_2O_3$  phase with space group  $Ia\bar{3}$  (DB# 01-081-9987) (Figure 4).



**Figure 4.** XRD patterns of the  $Y_xSr_{1.5-x}TiO_3$  reaction mixture powders ( $x = 0.2, 0.4, 0.6,$  and  $1$ ).

Standard diffraction patterns and 3D structural models of the RM components were generated using the Vesta software (Figure 5) to facilitate phase identification and visualization of crystal structures. The unit cell parameters of the starting powders matched calculated values for Rutile tetragonal phase with  $a = b = 4.5933$ ,  $c = 2.9592$  Å, Anatase tetragonal phase with  $a = b = 3.78520$ ,  $c = 9.51390$  Å, Yttrium Oxide cubic phase with  $a = b = c = 10.60410$  Å, and Strontianite orthorhombic phase with  $a = 6.02000$   $b = 5.09300$   $c = 8.37600$  Å.

As previously shown by dilatometry, XRD, TGA, and synchrotron XRD [39], the optimal sintering temperature for reaction sintering of RM based on  $SrCO_3$  and  $TiO_2$  to produce a single phase  $SrTiO_3$  perovskite ceramic via SPS was determined to be  $1300$  °C. The ceramic formation process occurred in three shrinkage stages of the RM: (1) particle rearrangement and packing under pressing pressure at low temperature; (2) in situ interaction of RM components, including partial decomposition of  $SrCO_3$ , and consolidation of the nascent  $SrTiO_3$  phase under thermal and pressing conditions; (3) deep interaction of RM components to form a single phase  $SrTiO_3$  composition and its consolidation via activation of solid state grain boundary diffusion and plastic flow above  $1270$  °C [39]. A similar dilatometric dependence was observed in the current study for  $Y_xSr_{1.5-x}TiO_3$  RM compositions (Figure 6). Specifically, sintering RM with 0.2 mole  $Y_2O_3$  content ( $Y_xSr_{1.5-x}TiO_3$ , where  $x = 0.2$ ) showed shrinkage at  $1000$  °C at a rate of  $0.6$  mm/min or more due to partial mechanical densification of RM particles and decomposition of strontium carbonate. The shrinkage rate then increased to  $1.4$  mm/min at  $1100$  °C associated with initiation of in situ interaction of RM components and partial formation of  $SrTiO_3$  perovskite and  $Y_2Ti_2O_7$  pyrochlore phases. This was corroborated using XRD data (Figure 7, curve 1). Increasing  $Y_2O_3$  content in the RM to 0.4 moles ( $Y_xSr_{1.5-x}TiO_3$ , where  $x = 0.4$ ) also led to a sharp increase in shrinkage rate to  $3.4$  mm/min at  $1100$  °C. However, further increasing  $Y_2O_3$  to 0.6 moles ( $Y_xSr_{1.5-x}TiO_3$ , where  $x = 0.6$ ) decreased the powder shrinkage rate to

1.6 mm/min. A similar trend of slowing shrinkage rate was observed upon full replacement of  $\text{Sr}^{2+}$  with  $\text{Y}^{3+}$  (sample  $\text{Y}_x\text{Sr}_{1.5-x}\text{TiO}_3$ , where  $x = 1$ ) not exceeding 1 mm/min. This is attributed to insufficient  $\text{SrCO}_3$  for the in situ reaction with  $\text{TiO}_2$  to form the  $\text{SrTiO}_3$  phase with  $a = b = c = 3.9046 \text{ \AA}$  and cell volume  $59.5292 \text{ \AA}^3$ . Per XRD, the ceramic composition consisted of a single  $\text{Y}_2\text{Ti}_2\text{O}_7$  phase with  $a = b = c = 10.0761 \text{ \AA}$  and cell volume  $1023.0085 \text{ \AA}^3$  (Figure 7, curve 4).

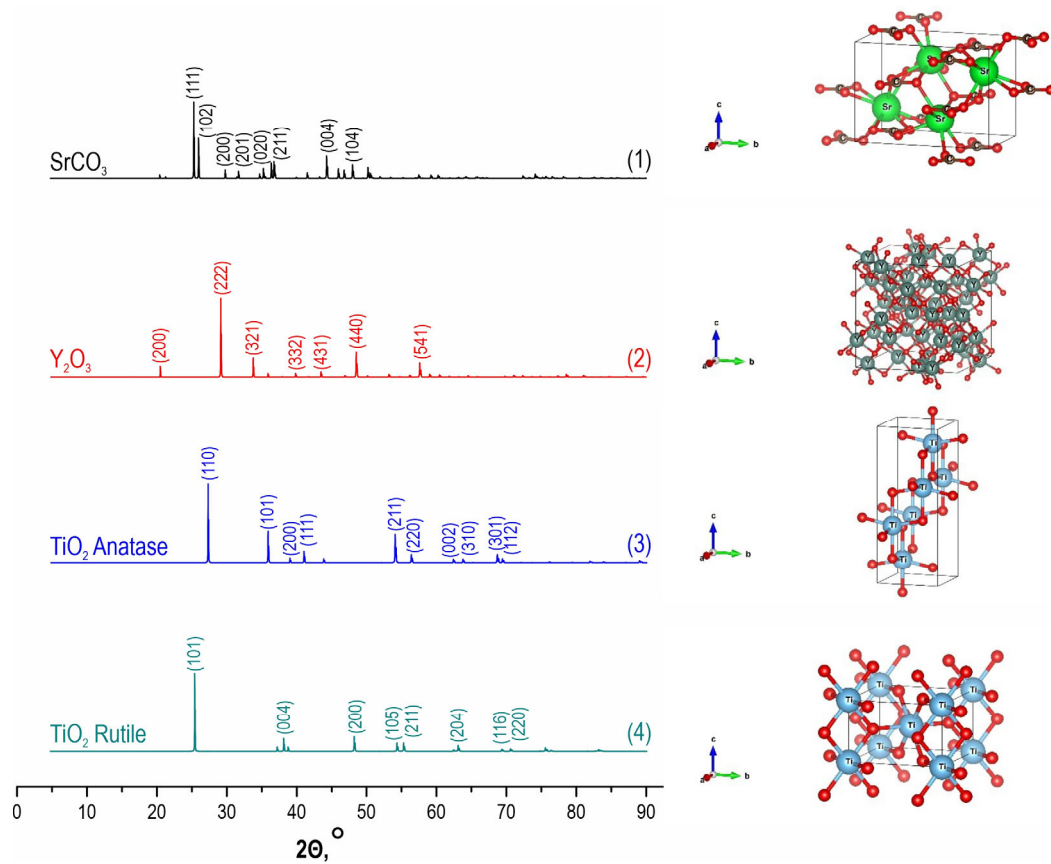


**Figure 5.** Standard diffraction patterns and crystal structure models of the RM components: (1)— $\text{SrCO}_3$ ; (2)— $\text{Y}_2\text{O}_3$ ; (3)— $\text{TiO}_2$  (anatase); (4)— $\text{TiO}_2$  (rutile).

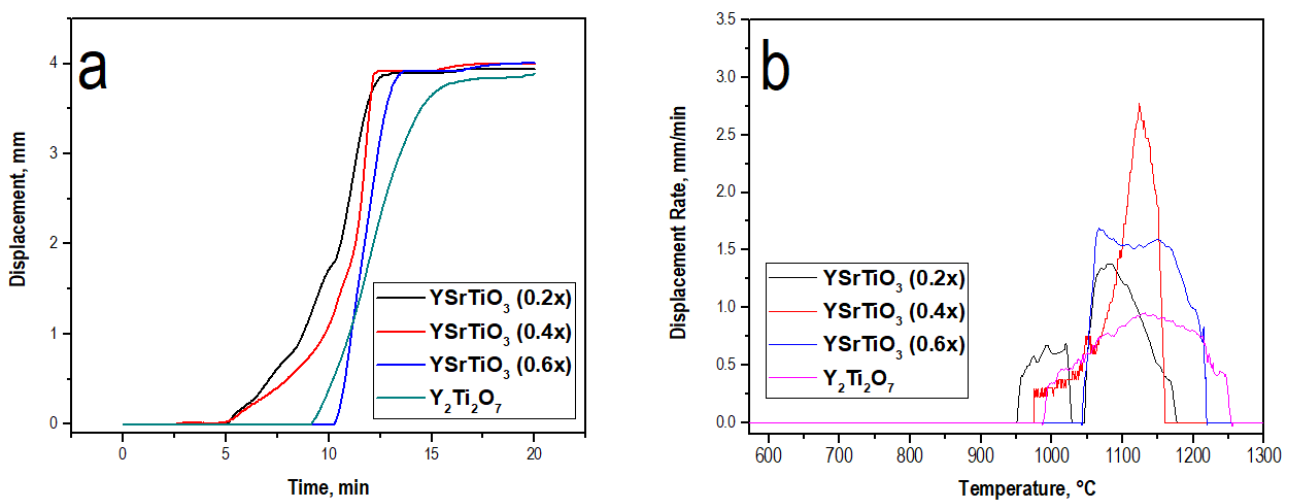


**Figure 6.** Dilatometric dependencies for RM powders: (a) shrinkage over time; (b) densification rate as a function of sintering temperature ( $T, P = \text{const}$ ).

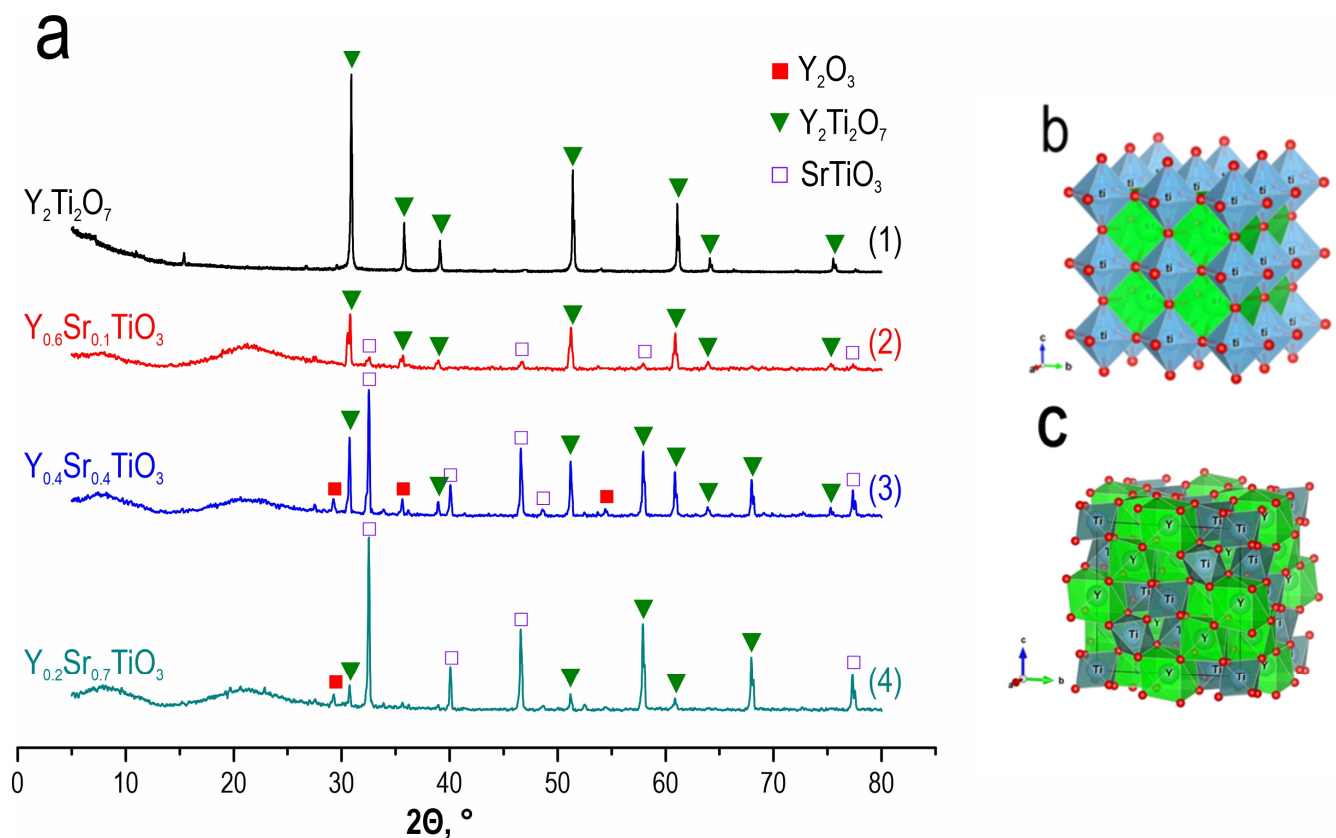


**Figure 7.** X-ray diffraction patterns (a) of composite ceramics fabricated by reaction SPS at 1300 °C using  $Y_xSr_{1-1.5x}TiO_3$  ( $x = 0.2, 0.4, 0.6$  and 1) RM powders, along with 3D crystal structure models of the perovskite  $SrTiO_3$  (b) and pyrochlore  $Y_2Ti_2O_7$  (c) phases.

The phases were quantified using the Rietveld method on TOPAS software (version 3) (Table 2). The calculated phase ratio using the Rietveld method shows that the initial compositions are selected correctly (Table 1), considering the error factor  $R_{wp}$ . The “goodnesses of fit” were 2.98, 2.26, 2.98, 3.08 for  $x = 0.2, 0.4, 0.6$ , and 1, respectively. As can be seen, the profile calculated using the Rietveld method has a small discrepancy with the experimental data.

**Table 2.** Phase content in the obtained samples calculated using the Rietveld method.

Sample Name	Phase Content, wt. %		$R_{wp}$ , %	GOE, %
	$SrTiO_3$	$Y_2Ti_2O_7$		
$Y_xSr_{1-1.5x}TiO_3$ , $x = 0.2$	84.44	15.56	4.56	2.98
$Y_xSr_{1-1.5x}TiO_3$ , $x = 0.4$	66.24	33.76	4.56	2.26
$Y_xSr_{1-1.5x}TiO_3$ , $x = 0.6$	94.08	5.92	4.68	2.98
$Y_xSr_{1-1.5x}TiO_3$ , $x = 1$	0	100	5.13	3.08

A detailed investigation of phase formation in the sintered RM system and the resulting composite ceramic was carried out using in situ synchrotron X-ray diffraction during heating up to 1000 °C (Figure 8). The diffraction patterns of  $Y_xSr_{1-1.5x}TiO_3$  RM compositions ( $x = 0.2, 0.4, 0.6$ ) showed diffraction peaks corresponding to  $SrCO_3$  phase (Figure 8a–c), consistent with XRD of the initial RMs (Figure 4). A decrease in  $SrCO_3$  peaks occurred over 850–900 °C, accompanied by the emergence of unidentified peaks near 29 and 34 ° that reached maxima around 900–950 °C. This correlates well with the DTA maximum at 941 °C seen previously [39]. These peaks likely relate to the rhombic → hexagonal phase

transition of  $\text{SrCO}_3$ .  $\text{SrO}$  peaks may also be present despite  $\text{SrCO}_3$  decomposition occurring at higher temperatures. Thus, conducting the in situ heating XRD experiment in air may have accelerated this process. Additionally, peaks for the final  $\text{SrTiO}_3$  perovskite phase emerge around 850–900 °C, in agreement with the literature [44]. It is also indicated that an intermediate  $\text{Sr}_2\text{TiO}_4$  phase forms, with decreasing intensity upon decreasing  $\text{SrCO}_3$  concentration in RM. The  $\text{Y}_2\text{Ti}_2\text{O}_7$  pyrochlore phase forms at 950 °C, observed for all RM compositions.  $\text{TiO}_2$  phases in the anatase and rutile forms, as well as some residual  $\text{Y}_2\text{O}_3$ , were also present for all RMs, attributed to the incomplete reaction of oxides by 1000 °C. As shown previously using XRD, heating the RMs to 1300 °C is optimal as it achieves a complete chemical reaction of the initial RM components.

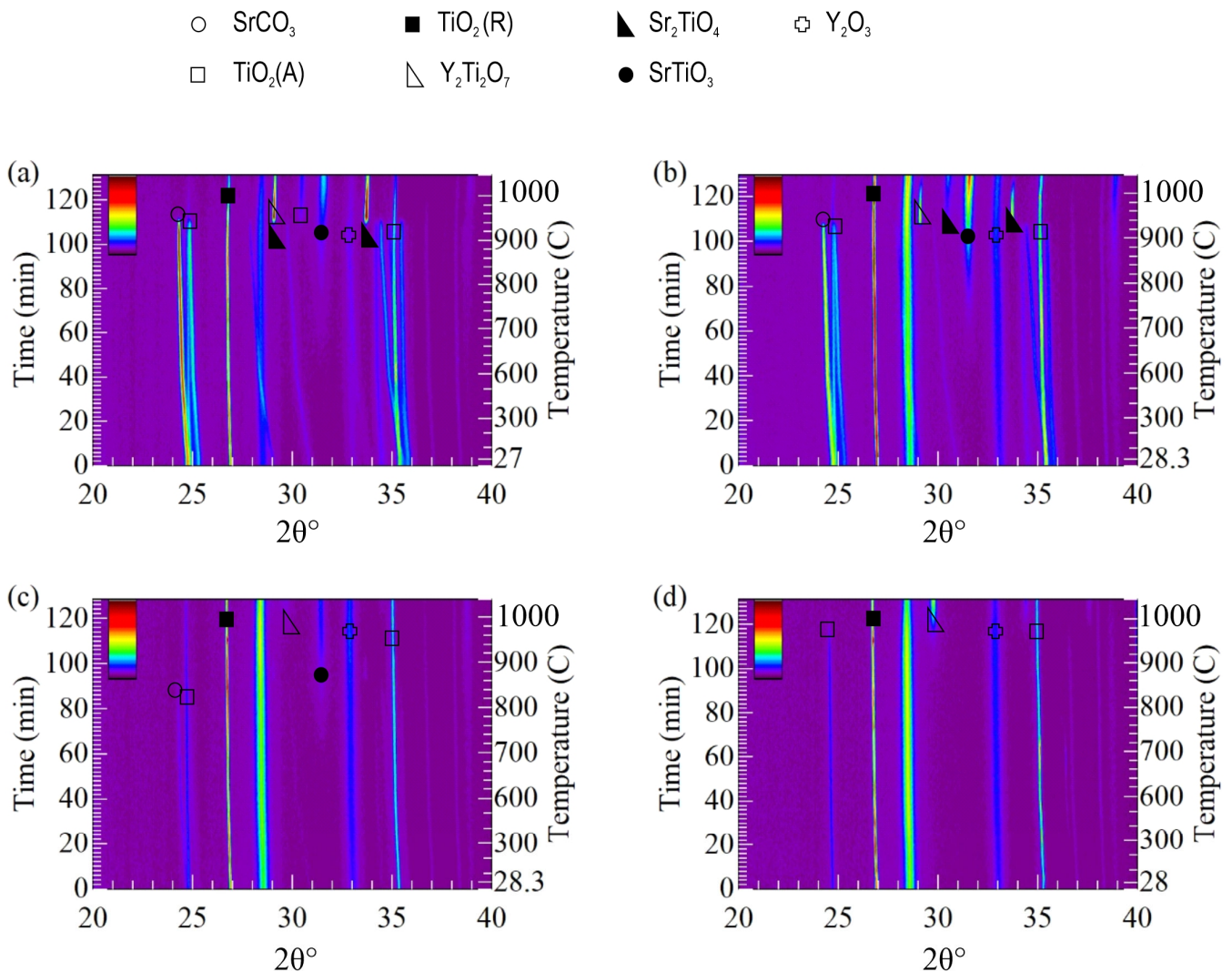


**Figure 8.** Synchrotron X-ray diffraction patterns of the in situ: interaction of components in  $\text{Y}_x\text{Sr}_{1-1.5x}\text{TiO}_3$  RM with  $x$  is: (a) 0.2; (b) 0.4; (c) 0.6; (d) 1.

SEM analysis (Figure 9) revealed that the microstructure of the fabricated ceramics consisted of densely sintered grains with no porosity or large defects. The morphology of longitudinal cross-sectional surfaces of composite ceramic samples (Figure 9a,a\*–d,d\*) was identical for all samples and exhibited a monolithic structure. For the single-phase sample fabricated without  $\text{SrCO}_3$ , a larger grain size was observed, likely related to the specific sintering behavior of the pyrochlore phase alone (Figure 9d,d\*). EDS analysis confirmed the component ratios in the original RM and resulting ceramics. The distribution of  $\text{Sr}^{2+}$ ,  $\text{Y}^{3+}$ , and  $\text{Ti}^{2+}$  was uniform across the cross-sectional surface areas analyzed (Figure 9).

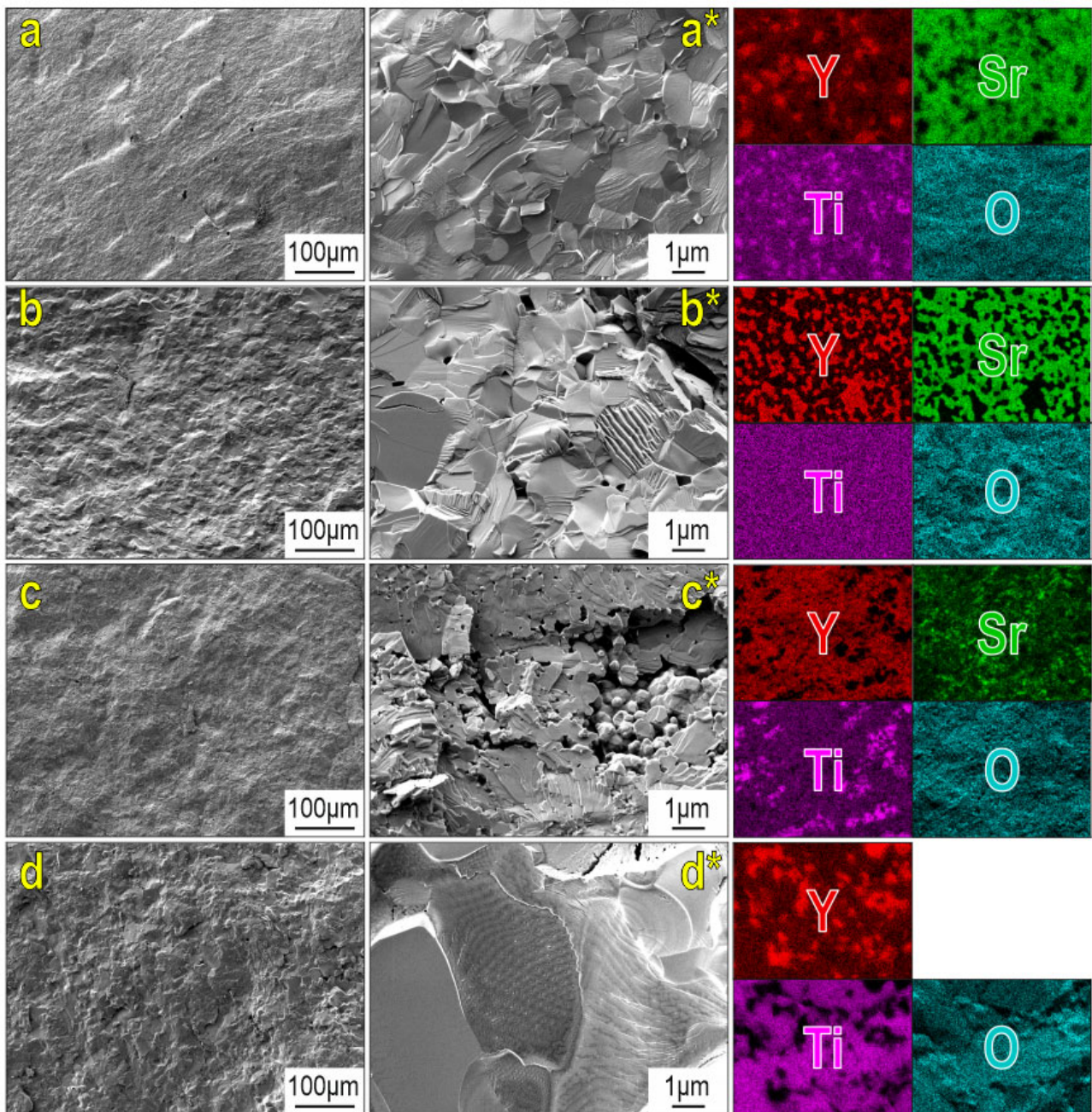


**Figure 9.** SEM images of longitudinal cross-sections of ceramics fabricated using SPS-RS at 1300 °C with compositions  $Y_xSr_{1-1.5x}TiO_3$ , where x is: (a)  $x = 0.2$ ; (b)  $x = 0.4$ ; (c)  $x = 0.6$ ; (d)  $x = 1$ .

The physical and mechanical properties of the ceramic samples were determined. It was found that relative density, compression strength, and Vickers microhardness varied depending on ceramic composition (Figure 10). With decreasing strontium concentration in  $Y_xSr_{1-1.5x}TiO_3$  for  $x = 0.4$  and above, the relative density of the ceramic slightly decreased (Figure 10a). Compression strength also decreased from 272.5 to 95.6 MPa, with the pyrochlore sample showing the minimum value compared to all test samples (Figure 10b). The reduction in properties is attributed to compositional changes in the ceramic samples, as the content of the  $Y_2Ti_2O_7$  pyrochlore phase increased. Pyrochlore has a lower Mohs hardness value (5–5.5) compared to  $SrTiO_3$  (6–6.5).

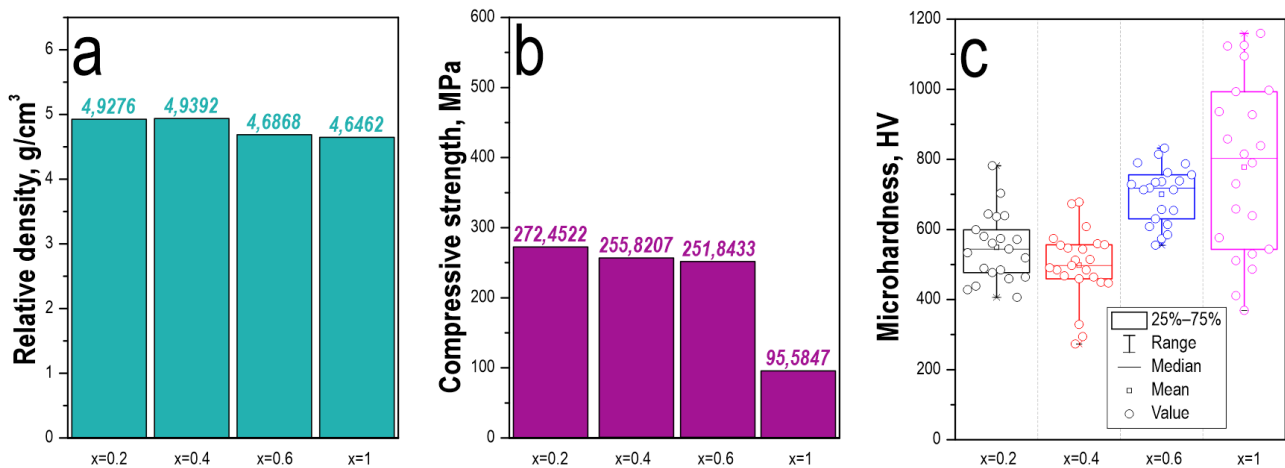


**Figure 10.** Physical and mechanical properties of  $Y_xSr_{1-1.5x}TiO_3$  ceramic samples fabricated using SPS-RS at 1300 °C: (a)—relative density of samples ( $g/cm^3$ ); (b)—compression strength (MPa); (c)—dispersion of Vickers microhardness (“box-and-whiskers” diagram) values on sample surfaces (HV).

A “box-and-whiskers” diagram of microhardness values was plotted to indirectly assess the strength micro-inhomogeneity of the material (Figure 10c). The data show that with changing ceramic composition, the hardness of ceramic materials changes only slightly in the range of 500–800 HV. Some scatter in microhardness values was observed for samples with a mixed  $SrTiO_3$  and  $Y_2Ti_2O_7$  composition, attributed to anisotropy in local volume regions of the material. For the sample consisting solely of the  $Y_2Ti_2O_7$  phase without  $SrTiO_3$ , this scatter was more significant. This is attributed to both the ceramic composition due to the lower Mohs hardness of the  $Y_2Ti_2O_7$  phase and its structure—larger grain growth during sintering was observed above for this phase alone.

An assessment of the hydrolytic stability of the fabricated composite ceramic samples was conducted, as this is a key parameter for their effectiveness in immobilizing radionuclides. It was determined that all samples exhibited low leaching rates of  $Sr^{2+}$  (Figure 11a). This value was  $10^{-5}$ – $10^{-6}$   $g \cdot cm^{-2} \cdot day^{-1}$ , meeting the requirements of GOST R 50926-96 for solidified high-level waste.

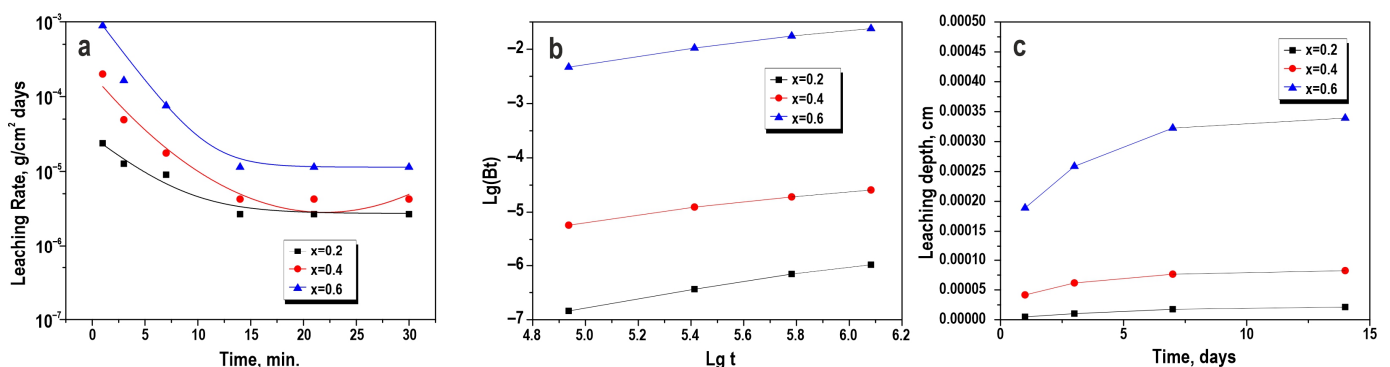


**Figure 11.** Hydrolytic stability of  $Y_xSr_{1-1.5x}TiO_3$  composite ceramic samples (where  $x = 0.2, 0.4, 0.6$ ) fabricated using SPS-RS at 1300 °C: (a)—leaching rate of  $Sr^{2+}$  from the ceramic volume; (b)—dependence of the logarithm of the leached  $Sr^{2+}$  fraction from the ceramic on the logarithm of the leaching time; (c)—dependence of the leaching depth on time.

The effective diffusion coefficient ( $D_e$ ) of  $Sr^{2+}$  in the consolidated ceramic sample, the leachability index, and matrix leaching depth were calculated using mathematical transformations of Fick’s second law according to the methodology described in reference [45], with results presented in Table 3. Additionally, in accordance with references [45,46], an

assessment of the dominant leaching mechanism was conducted. Following the de Groot and der Slot model [46], a dependence of the tangent of the inclination angle of the tangent line to the logarithmic dependence of the fraction of the leached component on the logarithm of time was plotted (Figure 11b), which relates to the matrix leaching mechanism. The results determined that the magnitude of the tangent of the inclination angle of the direct dependences remains unchanged over time. For the  $Y_xSr_{1-1.5x}TiO_3$  sample where  $x = 0.2$ , the tangent of the inclination angle was equal to 0.756, indicating strontium leaching predominantly by a surface dissolution mechanism. For  $Y_xSr_{1-1.5x}TiO_3$  samples where  $x = 0.4$  and 0.6, the tangents of the inclination angles were equal to 0.515 and 0.542, respectively, signifying strontium leaching primarily via a diffusional mechanism.

**Table 3.**  $Sr^{2+}$  leaching parameters on Day 30.

Sample Name	Diffusion Coefficient ( $D_e$ ), $cm^2/s$	Error, $cm^2/s$	Leachability Index (L)	Error	Leaching Depth, cm	Error, cm
$Y_xSr_{1-1.5x}TiO_3$ , $x = 0.2$	$8.81 \times 10^{-12}$	$\pm 0.44 \times 10^{-12}$	10.72	$\pm 0.53$	$3.00 \times 10^{-5}$	$\pm 0.15 \times 10^{-5}$
$Y_xSr_{1-1.5x}TiO_3$ , $x = 0.4$	$4.65 \times 10^{-11}$	$\pm 0.23 \times 10^{-11}$	9.86	$\pm 0.49$	$9.65 \times 10^{-5}$	$\pm 0.48 \times 10^{-5}$
$Y_xSr_{1-1.5x}TiO_3$ , $x = 0.6$	$5.44 \times 10^{-9}$	$\pm 0.27 \times 10^{-9}$	7.42	$\pm 0.37$	$3.76 \times 10^{-4}$	$\pm 0.18 \times 10^{-4}$

The leaching depth indicators (Figure 11c, Table 3) show that the fabricated materials are characterized by a high degree of stability in an aqueous environment, attributed to their chemical composition and dense microstructure. The leachability index (L) of  $Y_xSr_{1-1.5x}TiO_3$  samples where  $x = 0.2$  and 0.4 are above 8, allowing the conclusion that  $Sr^{2+}$  is reliably fixed within the ceramic volume. This characterizes the samples as promising for application as immobilizing matrices [47].

It was determined that the leaching rate of  $Y^{3+}$  from the ceramic volume was also within low limits, not exceeding  $10^{-5} g \cdot cm^{-2} \cdot day^{-1}$  (Figure 12a). A similar regularity was observed for the magnitudes of the tangent of the inclination angle of the tangent line to the dependence of the logarithm of the leached component fraction on the logarithm of time, which remained unchanged over time (Figure 12b). In addition, these values were identical for all samples and were 0.56. This indicates that the leaching rate of  $Y^{3+}$  is limited by its diffusion from the volume to the surface of the sample.

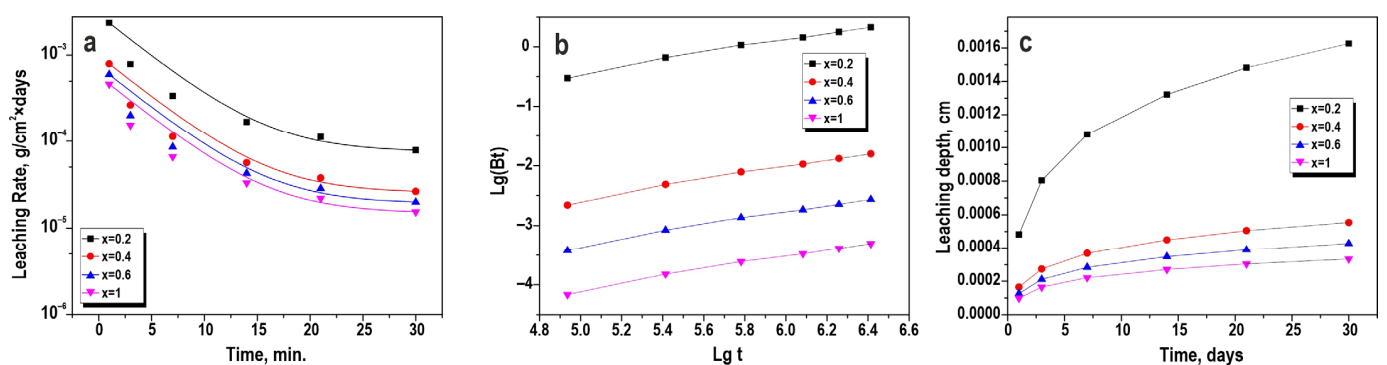


**Figure 12.** Hydrolytic stability of  $Y_xSr_{1-1.5x}TiO_3$  composite ceramic samples ( $x = 0.2, 0.4, 0.6$  and 1) fabricated using SPS-RS at  $1300^\circ C$ : (a)—leaching rate of  $Y^{3+}$  from the ceramic volume; (b)—dependence of the logarithm of the leached  $Y^{3+}$  fraction from the ceramic on the logarithm of the leaching time; (c)—dependence of the leaching depth on time.

The  $Y^{3+}$  diffusion coefficients (Table 4) in the ceramic samples varied significantly depending on the predominant cation in the ceramic composition. Presumably, increasing the  $Y^{3+}$  content stabilizes the structure of  $Y_2Ti_2O_7$ , increasing its strength of retention within the matrix volume.

**Table 4.** Yttrium leaching parameters on day 30.

Sample Name	Diffusion Coefficient ( $D_e$ ), $\text{cm}^2/\text{s}$	Error, $\text{cm}^2/\text{s}$	Leachability Index (L)	Error	Leaching Depth, cm	Error, cm
$\text{Y}_x\text{Sr}_{1-1.5x}\text{TiO}_3$ , $x = 0.2$	$7.37 \times 10^{-7}$	$\pm 0.36 \times 10^{-7}$	6.13	$\pm 0.3$	$1.63 \times 10^{-3}$	$\pm 0.08 \times 10^{-3}$
$\text{Y}_x\text{Sr}_{1-1.5x}\text{TiO}_3$ , $x = 0.4$	$1.30 \times 10^{-8}$	$\pm 0.06 \times 10^{-8}$	7.88	$\pm 0.39$	$5.54 \times 10^{-4}$	$\pm 0.27 \times 10^{-4}$
$\text{Y}_x\text{Sr}_{1-1.5x}\text{TiO}_3$ , $x = 0.6$	$3.51 \times 10^{-9}$	$\pm 0.17 \times 10^{-9}$	8.46	$\pm 0.42$	$4.27 \times 10^{-4}$	$\pm 0.21 \times 10^{-4}$
$\text{Y}_x\text{Sr}_{1-1.5x}\text{TiO}_3$ , $x = 1$	$8.86 \times 10^{-10}$	$\pm 0.44 \times 10^{-10}$	9.05	$\pm 0.45$	$3.34 \times 10^{-4}$	$\pm 0.16 \times 10^{-4}$

The leachability index (L) of  $\text{Y}_x\text{Sr}_{1-1.5x}\text{TiO}_3$  samples (Table 4) where  $x = 0.6$  and 1 are above 8, allowing the conclusion that  $\text{Y}^{3+}$  is reliably fixed within the ceramic volume.

Based on the obtained results of chemical resistance, as well as the composition of ceramics and its structure, it can be stated that an increase in the content of one of the presented phases leads to an increase in the rate of leaching from the ceramic volume of the component of the other phase. This is due to a number of factors, namely defects in the structure, which lead to an increase in the proportion of surface leaching of strontium due to an increase in the contact area with the solution. As indicated, the increase in the proportion of  $\text{Y}^{3+}$  leads to stabilization of the structure of pyrochlore  $\text{Y}_2\text{Ti}_2\text{O}_7$  and, consequently, to higher parameters of chemical stability. The opposite is also true for perovskite  $\text{SrTiO}_3$ . The high fraction of  $\text{Sr}^{2+}$  ions leads to the stabilization of the perovskite phase, which is consistent with the leaching and SEM data (Figures 9, 11 and 12).

#### 4. Conclusions

The work implemented a solid-state synthesis of mineral-like composite ceramics based on perovskite  $\text{SrTiO}_3$  and pyrochlore  $\text{Y}_2\text{Ti}_2\text{O}_7$ , promising for immobilization of radionuclides  $^{90}\text{Sr}$  and  $^{90}\text{Y}$ , as well as lanthanides and actinides. A study was conducted on the kinetics of sintering a reaction mixture composition of  $\text{Y}_x\text{Sr}_{1-1.5x}\text{TiO}_3$  ( $x = 0.2, 0.4, 0.6$ , and 1), as well as structural-phase changes in the resulting ceramics under spark plasma sintering conditions using XRD, SEM, EDS and in situ heating synchrotron XRD experiment methods. It was established that the formation of  $\text{SrTiO}_3$  begins already at  $850\text{ }^\circ\text{C}$  (although it cannot proceed intensely at this temperature), with the formation of an intermediate  $\text{Sr}_2\text{TiO}_4$  phase in the interval  $850\text{--}900\text{ }^\circ\text{C}$ , which was not determined by XRD data. The formation of the pyrochlore phase  $\text{Y}_2\text{Ti}_2\text{O}_7$  occurs at  $950\text{ }^\circ\text{C}$  and is observed for all the investigated RM compositions. A study of the densification dynamics of RM for the specified compositions was carried out at a constant temperature of  $1300\text{ }^\circ\text{C}$  and pressure of  $21.5\text{ MPa}$ , where it was shown that the in situ reactive interaction and simultaneous sintering of the initial powder mixture proceeds through three stages of densification: (1) regrouping and packing of particles of the initial powder under the influence of pressing; (2) decomposition of  $\text{SrCO}_3$  and formation of  $\text{SrTiO}_3$  and  $\text{Y}_2\text{Ti}_2\text{O}_7$  through possible intermediate products upon thermal effects above  $850\text{ }^\circ\text{C}$ ; (3) activation of diffusion, plastic deformation and viscous flow in the solid body at high heating of the sample above  $1270\text{ }^\circ\text{C}$ . It was determined that the resulting ceramics possess high physicomaterial characteristics: specific density of ceramics  $4.92\text{--}4.64\text{ g/cm}^3$ ; Vickers microhardness  $500\text{--}800\text{ HV}$ ; compression strength  $95.5\text{--}272.4\text{ MPa}$ . Variation of these characteristics depends on the composition and structure of the ceramics; in particular, their decrease is due to the increase in the content of the  $\text{Y}_2\text{Ti}_2\text{O}_7$  phase, which has a lower density on the Mohs scale compared to  $\text{SrTiO}_3$ . It has been proven that this ceramic has high hydrolytic stability, as the leaching rate of  $\text{Sr}^{2+}$  reaches  $10^{-6}\text{ g}\cdot\text{cm}^{-2}\cdot\text{day}$ , and  $\text{Y}^{3+}$   $10^{-5}\text{ g}\cdot\text{cm}^{-2}\cdot\text{day}$ , which meets the requirements of GOST R 50926-96 and ANSI/ANS 16.1 for solidified high-level wastes. The mechanism of leaching of these ions from the ceramic volume has been established, indicating diffusive leaching with minimal depth of diffusion of ions from the volume to the ceramic surface.

The applied result of the study is of interest for technologies of radioactive waste conditioning and the production of radioisotopic products.

**Author Contributions:** E.K.P.: Conceptualization, Resources, Writing—original draft. O.O.S.: Conceptualization, Project administration, Writing—original draft. A.A.B.: Writing—original draft. I.Y.B.: Writing—review and editing, Visualization. A.Z.: Investigation. S.A.A.: Investigation. A.N.F.: Investigation. Z.E.K.: Investigation. A.O.L.: Investigation. E.A.G.: Investigation. A.I.: Supervision, Writing—review and editing. I.G.T.: Supervision, Writing—review and editing. All authors have read and agreed to the published version of the manuscript.

**Funding:** The study was financially supported by the State Assignment of the Ministry of Science and Higher Education of the Russian Federation, topic No. FZNS-2023-0003. The equipment of the Joint Center for Collective Use, the interdisciplinary center in the field of nanotechnology, and new functional materials of the FEFU were used in the work (Vladivostok, Russia).

**Institutional Review Board Statement:** Not applicable.

**Informed Consent Statement:** Not applicable.

**Data Availability Statement:** There are no databases or archives. All obtained results are displayed in the publication.

**Conflicts of Interest:** The authors declare that they have no known competing financial interest or personal relationships that could have appeared to influence the work reported in this paper.

## References

1. Kurniawan, T.A.; Othman, M.H.D.; Singh, D.; Avtar, R.; Hwang, G.H.; Setiadi, T.; Lo, W. Technological Solutions for Long-Term Storage of Partially Used Nuclear Waste: A Critical Review. *Ann. Nucl. Energy* **2022**, *166*, 108736. [\[CrossRef\]](#)
2. Semenishchev, V.S.; Voronina, A.V. Isotopes of Strontium: Properties and Applications. In *Strontium Contamination in the Environment. The Handbook of Environmental Chemistry*; Springer: Cham, Switzerland, 2020; pp. 25–42.
3. Sun, Y.; Chmielewski, A.G. (Eds.) *Applications of Ionizing Radiation*, 1st ed.; Institute of Nuclear Chemistry and Technology: Warszawa, Poland, 2017; ISBN 978-83-933935-9-6.
4. Li, G.; Zhang, S.; Zhou, Y. A Review of Radioisotope Batteries. *Chinese Sci. Bull.* **2017**, *62*, 1831–1845. [\[CrossRef\]](#)
5. DeNardo, S.J.; DeNardo, G.L. Targeted Radionuclide Therapy for Solid Tumors: An Overview. *Int. J. Radiat. Oncol. Biol. Phys.* **2006**, *66*, 89–95. [\[CrossRef\]](#) [\[PubMed\]](#)
6. Silva, R.M.V.; Belinato, W.; Santos, W.S.; Souza, L.F.; Perini, A.P.; Neves, L.P.; Souza, D.N. Low Cost Electron Irradiator Using  $^{90}\text{Sr}+^{90}\text{Y}$  Sources. *Radiat. Phys. Chem.* **2020**, *167*, 108235. [\[CrossRef\]](#)
7. Vance, E.R. Ceramic Waste Forms. In *Comprehensive Nuclear Materials*; Elsevier: Amsterdam, The Netherlands, 2012; pp. 485–503.
8. Donald, I.W. *Waste Immobilization in Glass and Ceramic Based Hosts Radioactive, Toxic and Hazardous Wastes*; John Wiley & Sons Ltd: Chichester, UK, 2010; ISBN 978-1-444-31937-8.
9. Donald, I.W.; Metcalfe, B.L.; Taylor, R.N.J. Review The Immobilization of High Level Radioactive Wastes Using Ceramics and Glasses. *J. Mater. Sci.* **1997**, *32*, 5851–5887. [\[CrossRef\]](#)
10. Ravikumar, R.; Gopal, B. Structural Integrity of Cs and Sr Immobilized Lacunar Apatite Phosphate Simulated Ceramic Wasteform  $\text{Na}_{0.9}\text{Cs}_{0.1}\text{Pb}_3\text{Sr}(\text{PO}_4)_3$  under Heat and Aqueous Flow. *J. Nucl. Mater.* **2022**, *558*, 153388. [\[CrossRef\]](#)
11. Orlova, A.I. Crystalline Phosphates for HLW Immobilization—Composition, Structure, Properties and Production of Ceramics. Spark Plasma Sintering as a Promising Sintering Technology. *J. Nucl. Mater.* **2022**, *559*, 153407. [\[CrossRef\]](#)
12. Alekseeva, L.S.; Nokhrin, A.V.; Orlova, A.I.; Boldin, M.S.; Lantsev, E.A.; Murashov, A.A.; Korchenkin, K.K.; Ryabkov, D.V.; Chuvil'deev, V.N. Ceramics Based on the  $\text{NaRe}_2(\text{PO}_4)_3$  Phosphate with the Kosnarite Structure as Waste Forms for Technetium Immobilization. *Inorg. Mater.* **2022**, *58*, 325–332. [\[CrossRef\]](#)
13. Orlova, A.I.; Ojovan, M.I. Ceramic Mineral Waste-Forms for Nuclear Waste Immobilization. *Materials* **2019**, *12*, 2638. [\[CrossRef\]](#)
14. Ma, J.; Fang, Z.; Yang, X.; Wang, B.; Luo, F.; Zhao, X.; Wang, X.; Yang, Y. Investigating Hollandite–Perovskite Composite Ceramics as a Potential Waste Form for Immobilization of Radioactive Cesium and Strontium. *J. Mater. Sci.* **2021**, *56*, 9644–9654. [\[CrossRef\]](#)
15. Wang, J.; Zhan, L.; Wang, J.; Wen, J.; Fan, L.; Wu, L. Sr/Ce Co-Immobilization Evaluation and High Chemical Stability of Novel  $\text{Sr}_{0.5}\text{Zr}_2(\text{PO}_4)_3\text{-CePO}_4$  Composite Ceramics for Nuclear Waste Forms. *J. Aust. Ceram. Soc.* **2022**, *58*, 881–889. [\[CrossRef\]](#)
16. Ojovan, M.I.; Lee, W.E.; Kalmaykov, S.N. Ceramics and Novel Technologies. In *An Introduction to Nuclear Waste Immobilisation*; Elsevier: Amsterdam, The Netherlands, 2019; pp. 369–395.
17. Ojovan, M.I.; Lee, W.E. New Immobilising Hosts and Technologies. In *An Introduction to Nuclear Waste Immobilisation*; Elsevier: Amsterdam, The Netherlands, 2014; pp. 283–305.
18. Zhang, R.; Yang, J.; Yan, D.; Guo, Z.; Su, W. Consolidation of High-Level Radioactive Wastes into Strontium Titanate by CS Method. *Proc. Mater. Sci. Forum* **2012**, *704–705*, 625–630. [\[CrossRef\]](#)

19. Zhang, R.; Gao, Y.; Wang, J.; Li, L.; Su, W. Leaching Properties of Immobilization of HLW into SrTiO<sub>3</sub> Ceramics. *Adv. Mater. Res.* **2011**, *332–334*, 1807–1811. [[CrossRef](#)]
20. Zhang, K.; Wen, G.; Yin, D.; Zhang, H. Preparation and Aqueous Durability of Sr Incorporation into Rutile TiO<sub>2</sub>. *J. Wuhan Univ. Technol. Mater. Sci. Ed.* **2015**, *30*, 1179–1183. [[CrossRef](#)]
21. Mu, W.; Yu, Q.; Li, X.; Wei, H.; Jian, Y. Crystal Structure Stability of Simulated Sr<sub>1–1.5x</sub>Y<sub>x</sub>TiO<sub>3</sub> (x = 0–0.12) Waste Forms. *J. Wuhan Univ. Technol. Mater. Sci. Ed.* **2017**, *32*, 89–93. [[CrossRef](#)]
22. O'Brien, R.C.; Ambrosi, R.M.; Bannister, N.P.; Howe, S.D.; Atkinson, H.V. Safe Radioisotope Thermoelectric Generators and Heat Sources for Space Applications. *J. Nucl. Mater.* **2008**, *377*, 506–521. [[CrossRef](#)]
23. Tokita, M. Spark Plasma Sintering (SPS) Method, Systems, and Applications. In *Handbook of Advanced Ceramics*; Elsevier: Amsterdam, The Netherlands, 2013; pp. 1149–1177. [[CrossRef](#)]
24. Hu, Z.-Y.; Zhang, Z.-H.; Cheng, X.-W.; Wang, F.-C.; Zhang, Y.-F.; Li, S.-L. A Review of Multi-Physical Fields Induced Phenomena and Effects in Spark Plasma Sintering: Fundamentals and Applications. *Mater. Des.* **2020**, *191*, 108662. [[CrossRef](#)]
25. Olevsky, E.A.; Dudina, D.V. Field-Assisted Sintering: Science and Applications. In *Field-Assisted Sintering*; Springer: Basel, Switzerland, 2018; pp. 1–425. [[CrossRef](#)]
26. Huo, D.; Gosset, D.; Siméone, D.; Baldinozzi, G.; Khodja, H.; Villeroy, B.; Surblé, S. Influence of Sintering Methods on Microstructure and Ionic Conductivity of La<sub>1.95</sub>Sr<sub>0.05</sub>Zr<sub>2</sub>O<sub>6.975</sub> Synthesized by Co-Precipitation. *Solid State Ion.* **2015**, *278*, 181–185. [[CrossRef](#)]
27. Potanina, E.A.; Orlova, A.I.; Nokhrin, A.V.; Boldin, M.S.; Sakharov, N.V.; Belkin, O.A.; Chuvil'deev, V.N.; Tokarev, M.G.; Shotin, S.V.; Zelenov, A.Y. Characterization of Na<sub>x</sub>(Ca/Sr)<sub>1–2x</sub>Nd<sub>x</sub>WO<sub>4</sub> Complex Tungstates Fine-Grained Ceramics Obtained by Spark Plasma Sintering. *Ceram. Int.* **2018**, *44*, 4033–4044. [[CrossRef](#)]
28. Potanina, E.A.; Orlova, A.I.; Mikhailov, D.A.; Nokhrin, A.V.; Chuvil'deev, V.N.; Boldin, M.S.; Sakharov, N.V.; Lantsev, E.A.; Tokarev, M.G.; Murashov, A.A. Spark Plasma Sintering of Fine-Grained SrWO<sub>4</sub> and NaNd(WO<sub>4</sub>)<sub>2</sub> Tungstates Ceramics with the Scheelite Structure for Nuclear Waste Immobilization. *J. Alloys Compd.* **2019**, *774*, 182–190. [[CrossRef](#)]
29. Potanina, E.A.; Orlova, A.I.; Nokhrin, A.V.; Mikhailov, D.A.; Boldin, M.S.; Sakharov, N.V.; Belkin, O.A.; Lantsev, E.A.; Tokarev, M.G.; Chuvil'deev, V.N. Fine-Grained Tungstates SrWO<sub>4</sub> and NaNd(WO<sub>4</sub>)<sub>2</sub> with the Scheelite Structure Prepared by Spark Plasma Sintering. *Russ. J. Inorg. Chem.* **2019**, *64*, 296–302. [[CrossRef](#)]
30. Papynov, E.K.; Belov, A.A.; Shichalin, O.O.; Buravlev, I.Y.; Azon, S.A.; Golub, A.V.; Gerasimenko, A.V.; Parotkina, Y.; Zavjalov, A.P.; Tananaev, I.G.; et al. SrAl<sub>2</sub>Si<sub>2</sub>O<sub>8</sub> Ceramic Matrices for 90Sr Immobilization Obtained via Spark Plasma Sintering-Reactive Synthesis. *Nucl. Eng. Technol.* **2021**, *53*, 2289–2294. [[CrossRef](#)]
31. Savinykh, D.O.; Khainakov, S.A.; Boldin, M.S.; Orlova, A.I.; Aleksandrov, A.A.; Popov, A.A.; Murashov, A.A.; Garcia-Granda, S.; Nokhrin, A.V.; Chuvil'deev, V.N. Synthesis, Thermal Expansion Behavior and Sintering of Sodium Zirconium Nickel and Calcium Zirconium Nickel Phosphates. *Inorg. Mater.* **2021**, *57*, 529–540. [[CrossRef](#)]
32. Shu, X.; Chen, S.; Hou, C.; Xie, Y.; Zhang, H.; Li, B.; Yang, Y.; Wang, X.; Li, L.; Lu, X. Rapid Synthesis of Gd<sub>2</sub>Zr<sub>2</sub>O<sub>7</sub> Glass-Ceramics Using Spark Plasma Sintering. *J. Am. Ceram. Soc.* **2020**, *103*, 597–603. [[CrossRef](#)]
33. Wang, L.; Shu, X.; Yi, F.; Shao, D.; Zhang, K.; Zhang, H.; Lu, X. Rapid Fabrication and Phase Transition of Nd and Ce Co-Doped Gd<sub>2</sub>Zr<sub>2</sub>O<sub>7</sub> Ceramics by SPS. *J. Eur. Ceram. Soc.* **2018**, *38*, 2863–2870. [[CrossRef](#)]
34. He, N.; Wei, G.; Wen, P.; Han, W.; Xu, C.; Shu, X.; Luo, F.; Chen, S.; Wang, L.; Xie, Y.; et al. Effect of Improved Trialkyl Phosphine Oxides Waste Content on Phase Composition and Density of Spark Plasma Sintered Gd<sub>2</sub>Zr<sub>2</sub>O<sub>7</sub> Ceramics. *Int. J. Energy Res.* **2021**, *45*, 8724–8734. [[CrossRef](#)]
35. Luo, F.; Tang, H.; Shu, X.; Chen, Z.; Xu, C.; Wei, G.; Wu, D.; Chen, S.; Zhang, H.; Xie, Y.; et al. Immobilization of Simulated An<sup>3+</sup> into Synthetic Gd<sub>2</sub>Zr<sub>2</sub>O<sub>7</sub> Ceramic by SPS without Occupation or Valence Design. *Ceram. Int.* **2021**, *47*, 6329–6335. [[CrossRef](#)]
36. Shu, X.; Qing, Q.; Li, B.; Yang, Y.; Li, L.; Zhang, H.; Shao, D.; Lu, X. Rapid Immobilization of Complex Simulated Radionuclides by As-Prepared Gd<sub>2</sub>Zr<sub>2</sub>O<sub>7</sub> Ceramics without Structural Design. *J. Nucl. Mater.* **2019**, *526*, 151782. [[CrossRef](#)]
37. Papynov, E.K.; Belov, A.A.; Shichalin, O.O.; Buravlev, I.Y.; Azon, S.A.; Gridasova, E.A.; Parotkina, Y.A.; Yagofarov, V.Y.; Drankov, A.N.; Golub, A.V.; et al. Synthesis of Perovskite-Like SrTiO<sub>3</sub> Ceramics for Radioactive Strontium Immobilization by Spark Plasma Sintering-Reactive Synthesis. *Russ. J. Inorg. Chem.* **2021**, *66*, 645–653. [[CrossRef](#)]
38. Kosyanov, D.Y.; Yavetskiy, R.P.; Tolmachev, A.V.; Vornovskikh, A.A.; Pogodaev, A.V.; Gridasova, E.A.; Shichalin, O.O.; Kaidalova, T.A.; Kuryavyy, V.G. Fabrication of Highly-Doped Nd<sup>3+</sup>:YAG Transparent Ceramics by Reactive SPS. *Ceram. Int.* **2018**, *44*, 23145–23149. [[CrossRef](#)]
39. Shichalin, O.O.; Belov, A.A.; Zavyalov, A.P.; Papynov, E.K.; Azon, S.A.; Fedorets, A.N.; Buravlev, I.Y.; Balanov, M.I.; Tananaev, I.G.; Shi, Y.; et al. Reaction Synthesis of SrTiO<sub>3</sub> Mineral-like Ceramics for Strontium-90 Immobilization via Additional in-Situ Synchrotron Studies. *Ceram. Int.* **2022**, *48*, 19597–19605. [[CrossRef](#)]
40. Papynov, E.K.; Shichalin, O.O.; Belov, A.A.; Buravlev, I.Y.; Portnyagin, A.S.; Kozlov, A.G.; Gridasova, E.A.; Tananaev, I.G.; Sergienko, V.I. Ionizing Radiation Source-Open Type Fabrication Using Additive Technology and Spark Plasma Sintering. *Ceram. Int.* **2022**, *49*, 3083–3087. [[CrossRef](#)]
41. Niwa, E.; Sato, K.; Yashiro, K.; Mizusaki, J. High-Temperature Gravimetric Study on the Kinetics of the Formation of SrTiO<sub>3</sub> by Solid State Reaction of SrCO<sub>3</sub> and TiO<sub>2</sub>. *ECS Trans.* **2019**, *16*, 205–210. [[CrossRef](#)]
42. Evdokov, O.V.; Titov, V.M.; Tolochko, B.P.; Sharafutdinov, M.R. In Situ Time-Resolved Diffractometry at SSTRC. *Nucl. Instrum. Methods Phys. Res. Sect. A Accel. Spectrometers Detect. Assoc. Equip.* **2009**, *603*, 194–195. [[CrossRef](#)]

43. Piminov, P.A.; Baranov, G.N.; Bogomyagkov, A.V.; Berkaev, D.E.; Borin, V.M.; Dorokhov, V.L.; Karnaev, S.E.; Kiselev, V.A.; Levichev, E.B.; Meshkov, O.I.; et al. Synchrotron Radiation Research and Application at VEPP-4. *Phys. Procedia* **2016**, *84*, 19–26. [[CrossRef](#)]
44. Aulchenko, V.M.; Evdokov, O.V.; Kutovenko, V.D.; Pirogov, B.Y.; Sharafutdinov, M.R.; Titov, V.M.; Tolochko, B.P.; Vasiljev, A.V.; Zhogin, I.A.; Zhulanov, V.V. One-Coordinate X-Ray Detector OD-3M. *Nucl. Instrum. Methods Phys. Res. Sect. A Accel. Spectrometers Detect. Assoc. Equip.* **2009**, *603*, 76–79. [[CrossRef](#)]
45. Yarusova, S.B.; Shichalin, O.O.; Belov, A.A.; Azon, S.A.; Buravlev, I.Y.; Golub, A.V.; Mayorov, V.Y.; Gerasimenko, A.V.; Papynov, E.K.; Ivanets, A.I.; et al. Synthesis of Amorphous  $\text{KAlSi}_3\text{O}_8$  for Cesium Radionuclide Immobilization into Solid Matrices Using Spark Plasma Sintering Technique. *Ceram. Int.* **2022**, *48*, 3808–3817. [[CrossRef](#)]
46. De Groot, G.J.; van der Sloot, H.A. *Determination of Leaching Characteristics of Waste Materials Leading to Environmental Product Certification*; Proceedings of the ASTM Special Technical Publication; ASTM International: West Conshohocken, PA, USA, 1992.
47. Cioffi, R.; Pansini, M.; Caputo, D.; Colella, C. Evaluation of Mechanical and Leaching Properties of Cement-Based Solidified Materials Encapsulating Cd-Exchanged Natural Zeolites. *Environ. Technol.* **1996**, *17*, 1215–1224. [[CrossRef](#)]

**Disclaimer/Publisher’s Note:** The statements, opinions and data contained in all publications are solely those of the individual author(s) and contributor(s) and not of MDPI and/or the editor(s). MDPI and/or the editor(s) disclaim responsibility for any injury to people or property resulting from any ideas, methods, instructions or products referred to in the content.